ACS APPLIED NANO MATERIALS

www.acsanm.org

Article

N/P Co-Doped Nanowrinkled Carbon Spheres Enabling Robust Metal-Free Cathodes for High-Performance Zinc-Air Batteries

Jiasui Huang, Bowen Yao, Zhiyang Huang, Tayirjan Taylor Isimjan,* Lixia Wang,* and Xiulin Yang*

Cite This: https://doi.org/10.1021/acsanm.6c02496

Read Online

ACCESS | Metrics & More | Article Recommendations | Supporting Information

ABSTRACT: The pursuit of productive and resilient metal-free electrocatalysts for the oxygen reduction reaction (ORR) is imperative for realizing advanced zinc-air battery (ZAB) technologies. Herein, we report a nanowrinkled nitrogen/phosphorus codoped carbon sphere (CNP) synthesized via an in situ heteroatom incorporation followed by a pyrolysis strategy. The resulting catalyst uniformly distributes N and P dopants, enabling optimized defect density and enhanced electronic modulation. XPS analysis reveals abundant pyridinic (17.96%) and pyrrolic nitrogen (52.97%) species as key active sites, which promote favorable oxygen adsorption and accelerate charge-transfer kinetics. When integrated into a liquid ZAB, the CNP cathode achieves a high peak power density of 202.2 mW cm^{-2} and a specific capacity of 768.8 mA h g_{Zn}^{-1}, and flexible ZABs exhibit a peak power density of 67.5 mW cm^{-2} with steady output during mechanical deformation. This work reveals that synergistic N/P electronic regulation integrated with nanostructural design provides a viable route toward highly durable and efficient metal-free air cathodes.

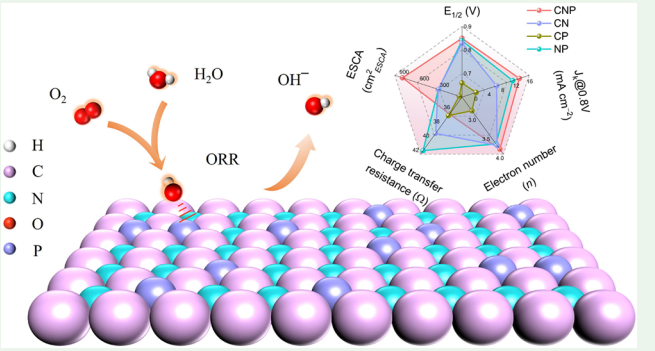

KEYWORDS: *electronic regulation, heteroatom doping, metal-free, oxygen reduction, zinc-air batteries*

1. INTRODUCTION

The global transition toward carbon-neutral economies has placed sustainable energy conversion and storage systems at the forefront of efforts to reconcile escalating energy demands with environmental sustainability.[1,2] Metal-air batteries are poised to become a cornerstone of next-generation clean energy, driven by their superior energy conversion efficiency.[3] Among them, zinc-air batteries (ZABs) stand out because of their high specific capacity, environmental sustainability, and economic feasibility, positioning them as ideal candidates for portable electronic devices, large-scale energy storage, and related applications.[4] However, the cathodic oxygen reduction reaction (ORR) in metal-air batteries is plagued by sluggish kinetics and low intrinsic activity. These drawbacks have evolved into a critical bottleneck that restricts the energy conversion efficiency and large-scale commercialization.[5] Conventional ORR catalysts are dominated by platinum-based materials. Although they exhibit superior catalytic activity, inherent limitations including scarcity, prohibitive cost, and limited durability render them incompatible with practical industrial deployment.[6,7] Accordingly, engineering affordable, earth-abundant electrocatalysts with exceptional ORR activity has become imperative in energy catalysis research.

In contemporary electrocatalysis research, nonprecious metal catalysts (e.g., Fe-, Co-, and Ni-based) have attracted considerable interest owing to their economic advantages and natural abundance.[8−10] However, during long-term continuous operation, these catalysts still face intractable challenges such as metal particle agglomeration and active site leaching,[11−13] which consequently reduce the active-site density and compromise catalytic durability. To surmount these constraints, nonmetallic carbon electrocatalysts have emerged as attractive candidates for ORR, capitalizing on their abundant precursors, tunable structures, and robust stability.[14,15] Nevertheless, pristine carbonaceous materials exhibit intrinsically modest ORR activity, necessitating deliberate modulation of their electronic configurations and nanoscale architectures to achieve satisfactory catalytic performance. Among diverse modification strategies for carbon materials, substitutional incorporation of heteroatoms (e.g., N, P, S) into carbon frameworks has been demonstrated to effectively modulate the electronic states and generate abundant active sites, thereby enhancing ORR activity.[15] Specifically, the incorporation of

Received: May 27, 2026
Revised: June 27, 2026
Accepted: July 12, 2026

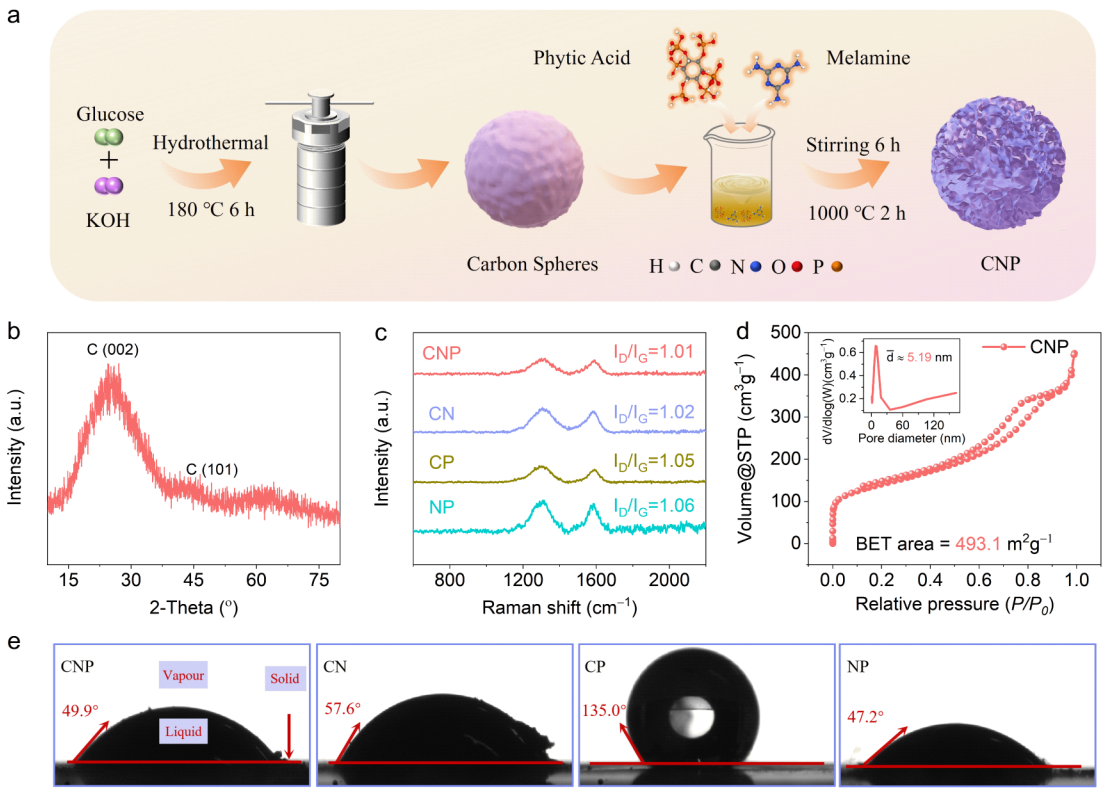

Figure 1. (a) Schematic diagram showing the preparation procedure of CNP catalyst. (b) XRD pattern of CNP. (c) Raman spectra of CNP and reference samples CN, CP, and NP. (d) N_2 adsorption−desorption isotherm measured for CNP and the inset presents the pore size distribution profile. (e) Contact angle test profiles of CNP, CN, CP, and NP.

nitrogen into the carbon matrix facilitates the rational adjustment of the abundance and distribution of active nitrogen species.[16] The higher electronegativity of pyridinic N relative to adjacent carbon atoms induces local charge redistribution, forming charge polarization centers that promote oxygen adsorption and thereby enhance catalytic activity.[17,18] In contrast, graphitic N modifies the surface electronic structure and improves electrical conductivity.[19,20] Furthermore, tailoring the pyrolysis temperature allows for precise control over both the total nitrogen content and configuration of nitrogen species, which in turn optimizes the adsorption energetics of oxygenated intermediates.[21] Although nitrogen doping has emerged as the most effective strategy for activating carbon-based materials, the activity of single-N-doped carbons remains inferior to that of Pt/C. The lower electronegativity (2.19) and larger atomic radius (110 pm) of phosphorus allow it to donate electrons to create complementary active sites and induce significant lattice distortion that generates abundant edge defects. These synergistic effects significantly accelerate ORR performance.[19,22] Furthermore, relative to conventional carbon frameworks, the nanowrinkled mesoporous structure provides a larger accessible surface area with more exposed defect sites and improved electrolyte penetration and mass transport, which collectively enhance the utilization of active sites.[23]

Based on the above considerations, this work utilizes structurally robust carbon spheres as precursors to fabricate a metal-free carbon-based ORR electrocatalyst via N/P codoping and high-temperature pyrolysis. N/P codoping synergistically modulates the carbon matrix's electronic structure, creates abundant active sites, and enhances electron transfer capability. Of greater significance, the as-fabricated CNP catalyst exhibits remarkable ORR performance, with a half-wave potential of 0.85 V and an onset potential of 1.01 V. As a result, when integrated as the air cathode catalyst, the CNP-based liquid ZAB achieves a peak power density of 202.2 mW cm^{-2} and a specific capacity of 768.8 mA h g_{Zn}^{-1}, outperforming commercial Pt/C (128.7 mW cm^{-2} and 698.9 mA h g_{Zn}^{-1}), and exhibits exceptional long-term stability exceeding 200 h. Furthermore, the CNP-based flexible ZAB delivers a higher peak power density (67.5 W cm^{-2}) than the Pt/C benchmark (49.6 mW cm^{-2}) and maintains stable output voltage under both flat and bent states.

2. RESULTS AND DISCUSSION

2.1. Synthesis and Structural Analysis of Catalysts

Figure 1a illustrates the synthetic preparation process of the CNP catalyst. Briefly, the synthesis of glucose carbon spheres was carried out by following previous work.[24] Subsequently, the obtained spheres were first mixed with melamine (MA) in deionized water, followed by the infusion of a specified amount of PA, after which the mixture was continuously agitated at ambient temperature for 6 h. Through in situ incorporation of N and P heteroatoms into carbon spheres, with subsequent pyrolysis at 1000 °C for 2 h under flowing N_2, a metal-free carbon-based catalyst codoped with nitrogen and phosphorus (CNP) was obtained. In this synthetic process, the abundant polyphosphate moieties in PA not only give rise to uniform in situ phosphorus doping but also establish a robust cross-linked network with melamine and the carbon sphere precursor, facilitating the formation of a mesoporous architecture during pyrolysis, ultimately enhancing the accessible surface area and

https://doi.org/10.1021/acsanm.6c02496
ACS Appl. Nano Mater. XXXX, XXX, XXX−XXX

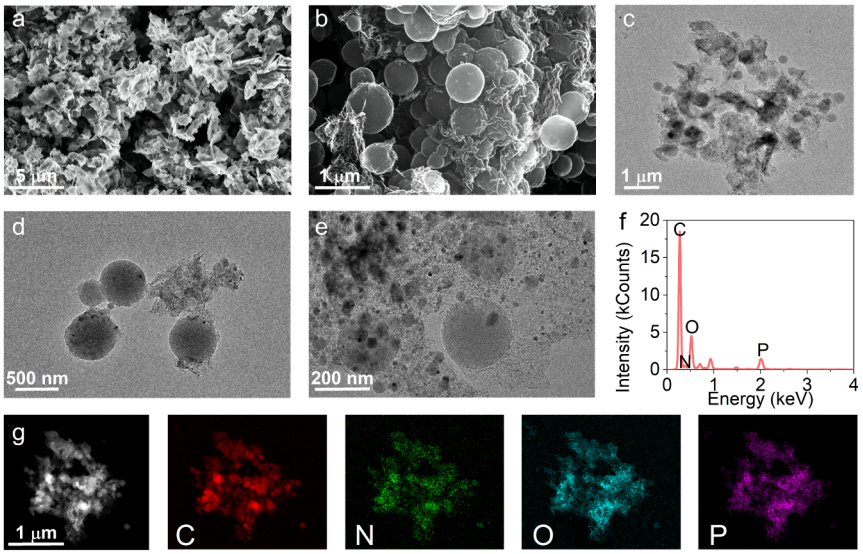

Figure 2. (a) SEM image of the CNP precursor before calcination. (b) SEM image, (c) TEM image, (d-e) HR-TEM images, (f) EDS spectrum profile, and (g) HAADF-STEM image with the corresponding elemental mapping images of CNP.

expediting ion migration.[25,26] X-ray powder diffraction (XRD) characterization reveals the prevalence of sp^2 -hybridized carbon domains within the as-synthesized material, as shown in Figure 1b and Figure S1. The two broad diffraction peaks detected at approximately 25° and 44° are assigned to the (002) and (101) crystal planes of graphite, respectively, which are identical with the samples prepared from the carbon sphere precursor, indicating preserved structural ordering after high-temperature treatment.[27,28] The Raman spectrum of CNP exhibits a defect-derived D-band at 1310 cm^{-1} and sp^2-hybridized vibrational G-band at around 1589 cm^{-1} (Figure 1c).[29] The I_D/I_G value is widely regarded as an indicator for evaluating the degree of defect or graphitization.[30] The control samples exhibit higher I_D/I_G ratios and more defects, which is attributed to the volatilization of nitrogen and phosphorus during high-temperature pyrolysis. In contrast, CNP shows a slightly lower I_D/I_G ratio due to its higher degree of carbon graphitization.[31] Given the fact that P atoms possess a larger radius (110 ppm) than C atoms (77 ppm), while N atoms (75 ppm) approximate that of C, the incorporation of P atoms can therefore introduce lattice distortion in the adjacent carbon framework, resulting in an increased defect density.[32,33] Therefore, the I_D/I_G value of CP (1.05) is slightly higher than that of CN (1.02). Moreover, Raman spectra of samples with varying PA concentrations show that the D-band intensity increases with PA content (Figure S2). Furthermore, the degree of graphitization rises correspondingly with increasing pyrolysis temperature. The N_2 adsorption/desorption isotherm was employed to evaluate the specific surface area and porosity of the synthesized catalysts. The N_2 adsorption/desorption isotherm curves reveal a specific surface area of 493.1 $m^2\ g^{-1}$ (Figure 1d), which is larger than those of CN (404.1 $m^2\ g^{-1}$) and CP (475.3 $m^2\ g^{-1}$), yet lower than that of NP (698.8 $m^2\ g^{-1}$) (Figure S4), which might be attributed to the shrinkage and reconstruction of the carbon matrix at high temperatures.[32,34,35] Moreover, the embedded pore-size distribution curve demonstrates that CNP features a hierarchical mesoporous architecture with an average pore size of 5.19 nm. Benefiting from a remarkably high specific surface area and proper porous architecture, CNP delivers abundant active sites and facilitates superior electron/mass transport in the ORR process.[36,37] In addition, surface wettability analysis further supports the enhanced catalytic interface. The contact angle of CNP is 49.9°, significantly lower than that of CP (135.0°) and comparable to CN (57.6°) (Figure 1e). This result demonstrates that incorporating nitrogen-based functional moieties markedly improves surface wettability, thereby promoting rapid electrolyte permeation, facilitating fast O_2 adsorption/desorption, and reducing mass transfer resistance.[38,39]

Scanning electron microscopy (SEM) together with transmission electron microscopy (TEM) was used to characterize the morphological features and structural properties of the catalysts. As shown in Figure 2a, mixed multilayer aggregates assembled from carbon-sphere precursors undergo carbonization and surface etching during high-temperature pyrolysis. This process results in the formation of a nanoscale crinkled carbon layer on the surface of the carbon spheres (Figure 2b). Concurrently, the thermal decomposition of PA engenders the release of CO_2, H_2O, and phosphorus oxides, which function as in situ porogens to generate a mesoporous structure.[40,41] Furthermore, thermal shrinkage induces anisotropic surface contraction, transforming carbon spheres into nanowrinkled architectures.[42] This morphological transformation is attributed to thermal shrinkage and heteroatom-induced lattice reconstruction during the carbonization. TEM and HR-TEM images (Figure 2c–e) further verify that following high-temperature pyrolysis, nitrogen and phosphorus species are uniformly incorporated onto the surface of the carbon spheres, while the carbon spheres retain their original integral morphology. The EDS spectrum profile further affirmed the existence of C, N, O, and P elements throughout the CNP catalyst (Figure 2f). As revealed by the elemental mapping images (Figure 2g), C, N, and P are uniformly dispersed across the entire carbon framework, which further confirms the effective incorporation of both N and P into the carbon matrix. Notably, while the carbon spheres serve as the robust structural skeleton and conductive support, the nanowrinkled structure provides abundant edge exposure. Moreover, the active components of CNP are the synergistic N/P-codoped

https://doi.org/10.1021/acsanm.6c02496
ACS Appl. Nano Mater. XXXX, XXX, XXX−XXX

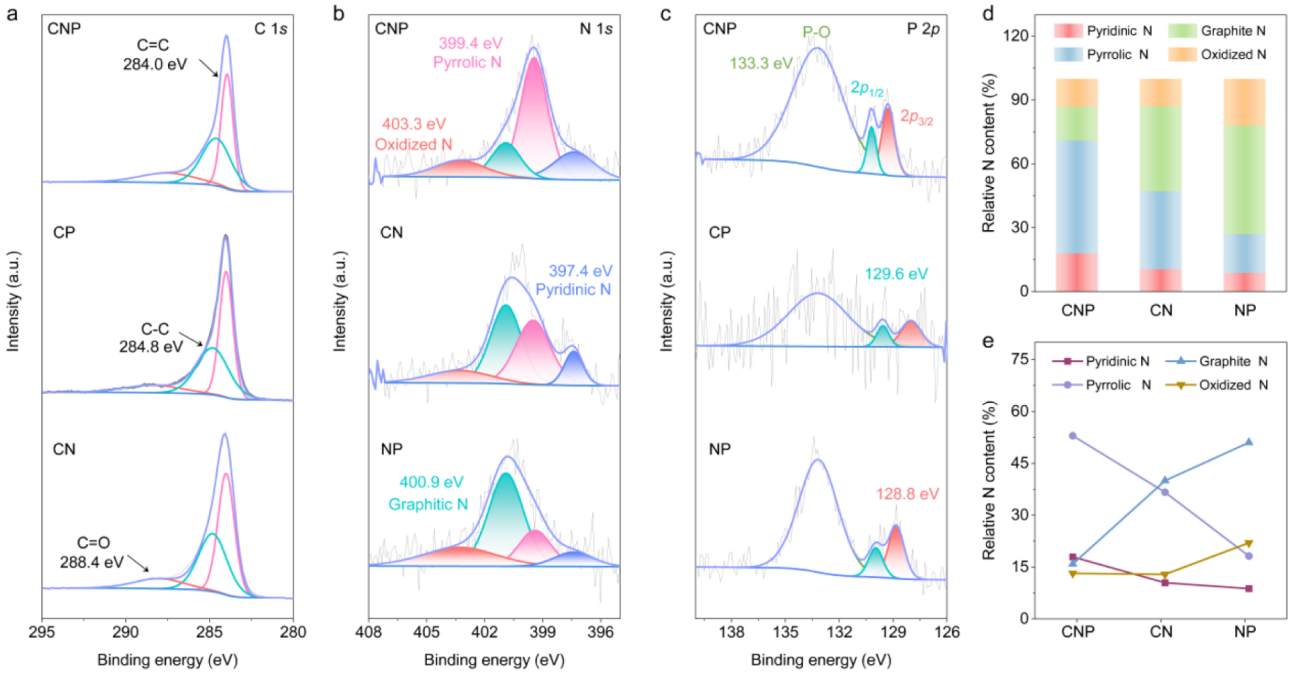

Figure 3. XPS spectra of CNP, CN, CP, and NP: (a) C 1*s*, (b) N 1*s*, (c) P 2*p*, (d) and (e) comparison histograms of the content (%) of different nitrogen species.

defective sites within this carbon architecture, and such uniform heteroatom distribution is critical for ensuring consistent electronic modulation across the catalyst surface, thereby enhancing ORR activity and stability.

X-ray photoelectron spectroscopy (XPS) was performed to elucidate the surface elemental composition and chemical states of the catalyst. Deconvolution performed on the C 1*s* spectral profiles of the synthesized CNP, CN, and CP (Figure 3a) resolved three signature peaks positioned at 284.0 eV (C═C), 284.8 eV (C−C), and 288.4 eV (C═O), respectively.[41] The dominant C═C/C−C contributions confirm the preservation of a graphitic carbon framework after high-temperature treatment, while the presence of C═O indicates residual oxygen-containing functional groups that may contribute to surface polarity and interfacial interactions. The high-resolution N 1*s* spectra in Figure 3b can be resolved into four components, corresponding to pyridinic N (397.4 eV), pyrrolic N (399.4 eV), graphitic N (400.9 eV), and oxidized N (403.3 eV).[43,44] Furthermore, XPS analysis indicates a predominance of pyridinic and pyrrolic nitrogen, accounting for 17.96% and 52.97%, respectively (Figure 3d-e and Table S1). Abundant pyridinic N plays a crucial catalytic role by inducing charge redistribution in adjacent carbon atoms, generating positively polarized carbon sites that facilitate O_2 adsorption and lower the ORR activation barrier.[45] On the other hand, pyrrolic N modulates the binding strength of oxygen intermediates, thereby promoting efficient adsorption/desorption dynamics during the reaction.[46] Meanwhile, graphitic N improves electrical conductivity by tuning the electronic configuration of the carbon lattice, further supporting rapid charge transfer.[14] Therefore, a high pyridine/pyrrole nitrogen content contributes significantly to the enhanced ORR activity by optimizing both adsorption energetics and reaction kinetics. The P 2*p* spectra (Figure 3c) exhibit two prominent peaks at 128.8 and 129.6 eV, assigned to P $2p_{3/2}$ and P $2p_{1/2}$, respectively, confirming successful phosphorus incorporation into the carbon framework.[9,47] Moreover, a weak peak observed at 133.3 eV arises from P−O bonds, originating from surface oxidation.[48,49] Phosphorus doping introduces lattice distortion due to its larger atomic radius, thereby modifying local electron density and creating defect-associated active sites. This electronic perturbation synergizes with nitrogen doping to regulate charge distribution and enhance ORR catalytic performance. Overall, the XPS results confirm successful and uniform N/P codoping, effective electronic structure modulation, and the formation of catalytically favorable nitrogen configurations, collectively underpinning the superior electrocatalytic activity of the CNP catalyst.

2.2. ORR Activities in Alkaline Medium

The ORR performance of the synthesized catalysts was evaluated in a 0.1 M KOH electrolyte with a standard three-electrode configuration. The catalyst synthesis process was optimized by tuning the MA dosage (Figure S5), PA loading (Figure S6) and pyrolysis temperature (Figure S7). Meanwhile, the larger atomic radius of P induces lattice distortion, which greatly elevates the density of structural defects (Figure S2). Nevertheless, diminished PA loadings result in insufficient P doping and limited porosity, whereas excessive PA provokes overetching and structural degradation.[50,51] In contrast, elevated pyrolysis temperatures improve graphitization and structural ordering (Figure S3) but concurrently and inevitably trigger the thermal depletion of active nitrogen dopants and active site structural collapse, which drastically weakens electrochemical ORR activity.[52,53] Accordingly, 1000 °C is determined to be the optimal pyrolysis temperature, achieving a compromise between carbon graphitization (I_D/I_G = 1.01) and the retention of active nitrogen species. Therefore, the CNP sample prepared with 1 g MA, 1.5 mL PA, and pyrolyzed at 1000 °C exhibited the best catalytic performance, delivering the most positive half-wave potential $E_{1/2}$, the highest limiting current density, and the lowest Tafel slope. As shown in Figure

https://doi.org/10.1021/acsanm.6c02496
ACS Appl. Nano Mater. XXXX, XXX, XXX−XXX

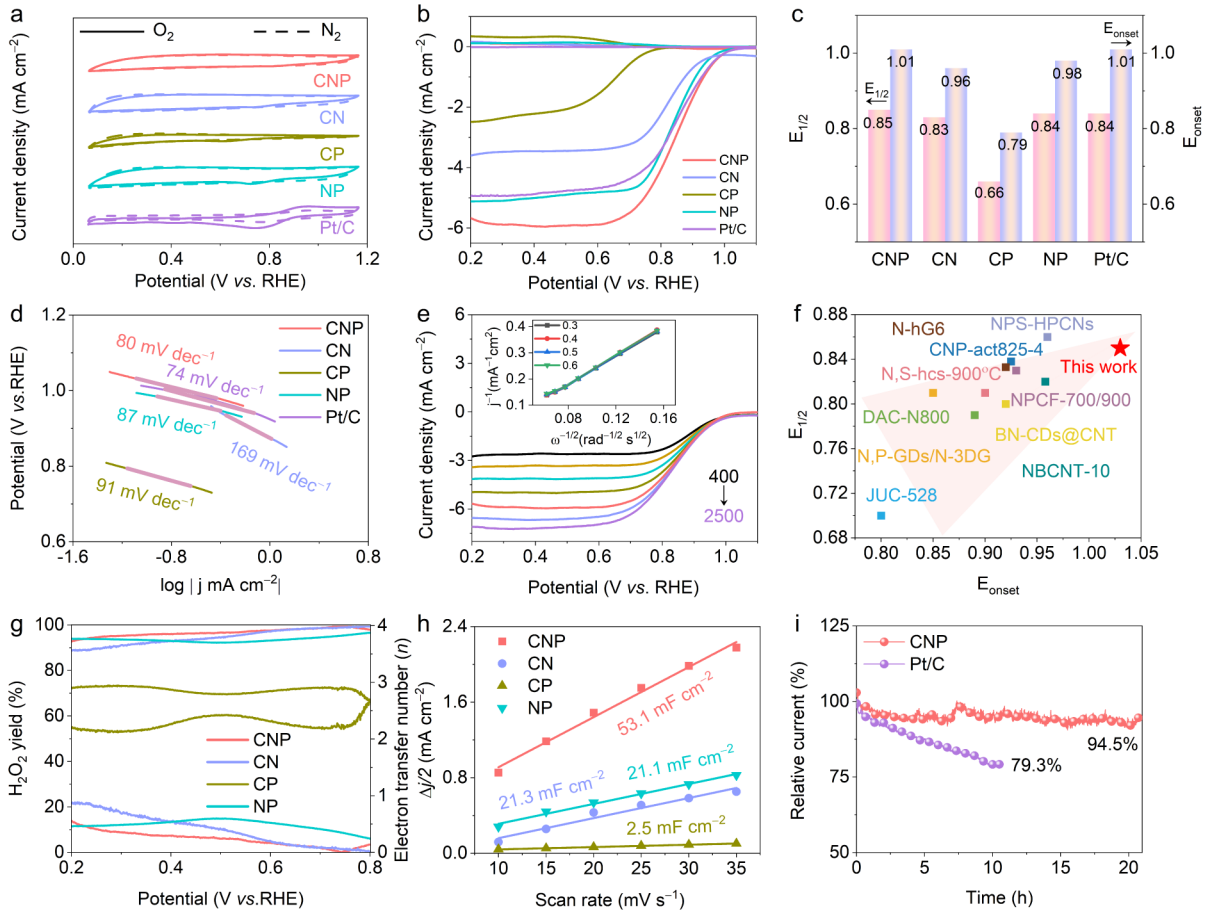

Figure 4. Electrochemical performance of different catalysts. (a) CV curves. (b) RRDE polarization curves at 1600 rpm. (c) Comparison of onset potential (E_{onset}) and half-wave potential ($E_{1/2}$). (d) Tafel slope. (e) LSV curves at different rotation speeds (400 to 2500 rpm), with the corresponding K-L plots (inset). (f) Comparison of E_{onset} and $E_{1/2}$ of CNP with those of other recently reported ORR catalysts. (g) H_2O_2 yield (%) and electron transfer number (n). (h) C_{dl} values. (i) Stability test of CNP and Pt/C.

4a, CNP displays a more positive oxygen reduction peak compared with CN, CP, NP, and 20 wt % commercial Pt/C, indicating enhanced catalytic activity. RRDE polarization curves presented in Figure 4b reveal that N/P codoping induces positive shifts in both the onset potential (1.01 V) and half-wave potential (0.85 V), which are comparable to Pt/C (1.01 V, 0.84 V) and superior to the control samples, confirming the beneficial electronic modulation introduced by heteroatom incorporation. As illustrated in Figure 4c, CNP exhibits notably higher onset and half-wave potentials compared to the control sample and approaches the benchmark Pt/C performance, indicating more favorable ORR kinetics. The Tafel slope of CNP (80 mV dec^{-1}) is significantly lower than those of CN (169 mV dec^{-1}), CP (91 mV dec^{-1}), and NP (87 mV dec^{-1}) and approaches that of Pt/C (74 mV dec^{-1}) (Figure 4d), demonstrating accelerated reaction kinetics.[51] This kinetic improvement arises from the synergistic N/P codoping, where pyridinic and pyrrolic nitrogen modulate the electronic distribution of neighboring carbon sites, lowering the energy barrier for oxygen adsorption and optimizing the binding strength of reaction intermediates.[54] Phosphorus possesses a larger atomic radius; its doping induces lattice distortion and abundant edge defects, as reflected by the elevated I_D/I_G ratio from Raman characterization. The defects generated by phosphorus doping disrupt the electrical neutrality of the carbon matrix and remarkably accelerate the interfacial charge transfer rate. The synergistic catalytic effect derived from N, P codoping endows CNP with both outstanding intrinsic catalytic activity and a high density of accessible active sites, which delivers superior ORR kinetic performance relative to monodoped catalysts.[55] To better evaluate its intrinsic activity, the kinetic current density (J_k) at 0.8 V was calculated. CNP achieves a J_k of 13.1 mA cm^{-2}, which is 2.08, 62.38, and 1.18 times higher than those of CN, CP, and NP, respectively (Table S2), indicating substantially enhanced intrinsic activity. The electron-transfer number (n) was derived from the Koutecky–Levich (K-L) equation. The K-L plot (Figure 4e) indicates that CNP undergoes a nearly four-electron transfer, exceeding that of the comparison samples (Figure S8, Table S2). As shown in Figure 4f and Table S2, CNP exhibits the most positive onset and half-wave potentials among the recently reported metal-free ORR catalysts. The RRDE measurements further confirm a dominant four-electron pathway, with a lower H_2O_2 yield and an average electron-transfer number of 3.87 (Figure 4g), demonstrating efficient and selective ORR kinetics. Furthermore, the electrochemically active surface area (ECSA) was estimated using the double-layer capacitance (C_{dl}) derived from CV profiles acquired in the non-Faradaic region (Figure S9) to estimate the electrochemically active surface area (ECSA). As shown in Figure 4h and Figure S10a, CNP exhibits significantly higher C_{dl} (53.1 mF cm^{-2}) and ESCA

https://doi.org/10.1021/acsanm.6c02496
ACS Appl. Nano Mater. XXXX, XXX, XXX−XXX

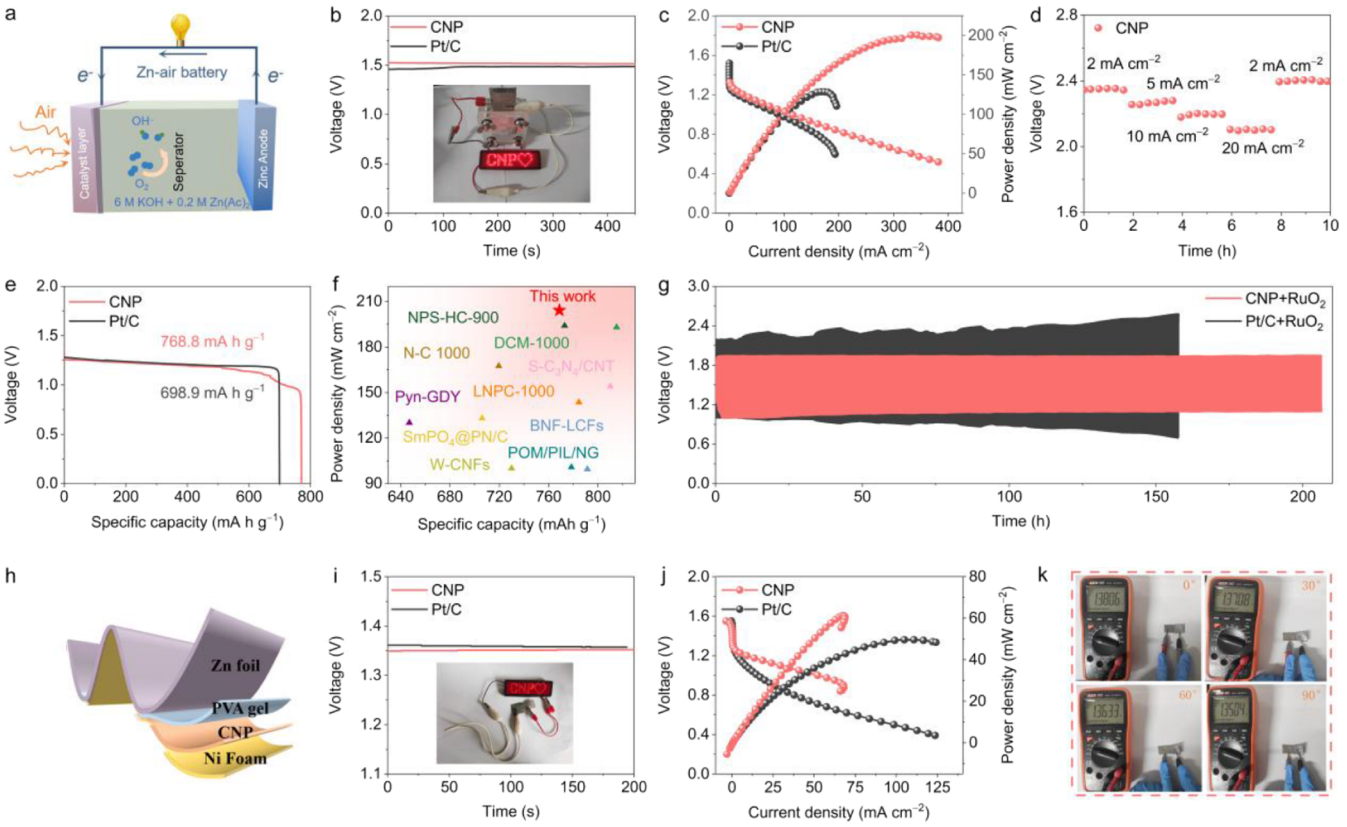

Figure 5. Performances of liquid and flexible ZABs. (a) Schematic diagram of a liquid ZAB. (b) OCV curves with the inset image of the assembled liquid ZAB powering an LED panel. (c) Discharge polarization curves and power density. (d) Discharge curves at different current densities. (e) Specific capacity plots. (f) Comparison of CNP-based ZAB with other recently reported metal-free ORR catalysts. (g) Galvanostatic cycling at 5 mA cm^{-2} of CNP+RuO_2 and Pt/C+RuO_2-based ZABs (20 min per cycle). (h) Schematic diagram of a flexible ZAB. (i) OCV curves with the inset image of the assembled flexible ZAB powering an LED panel. (j) Discharge polarization curves and power density of assembled flexible ZABs. (k) Output voltage at different bending angles.

(885 cm^2) values than all the comparison samples, indicating greater exposure of active sites. This enhancement arises from the synergistic N and P codoping, which increases defect density, optimizes porosity, and improves surface accessibility.[55] Electrochemical impedance spectroscopy (EIS) reveals that CNP exhibits a lower charge-transfer resistance (36.4 Ω) than the reference samples (Figure S10b), facilitating faster interfacial electron transfer and improved ORR kinetics.[56] Methanol tolerance tests were performed to assess the intrinsic ORR selectivity against competing methanol oxidation. Upon rapidly injecting 3 M methanol into the 0.1 M KOH electrolyte, the benchmark Pt/C catalyst undergoes a drastic current density decay, whereas the CNP catalyst sustains a nearly unaltered current response (Figure S11). This distinct contrast underscores the superior antipoisoning capability of CNP, reflecting its potential for versatile application in both metal-air batteries and direct methanol fuel cells.[57] Moreover, long-term durability tests further highlight the robustness of CNP. After 20 h of continuous operation, CNP retains 94.5% of its initial current, significantly outperforming commercial Pt/C, which retains only 79.3% after 10 h (Figure 4i). A further comparison with the reference samples (CN, CP, and NP), which retain only 79.1%, 66.6%, and 76.1% after 9 h, respectively (Figure S12), underscores the superior stability of CNP. To gain further insights into the structural and compositional robustness of CNP after the long-term durability test, we systematically characterized the catalyst. As illustrated in Figure S13, the XRD pattern of CNP exhibits negligible shifts in peak position and intensity relative to the pristine sample.[58,59] SEM images (Figure S14) disclose that the catalyst retains its nanowrinkled spherical morphology without severe aggregation or corrosion of the carbon substrate. In addition, XPS spectra (Figure S15) exhibit marginal variations in nitrogen content, originating from oxygen intermediates adsorbed onto the catalyst surface. The enhanced stability of CNP is primarily attributed to the synergistic effect of N/P codoping, which elevates the graphitization degree and structural ordering while maintaining defect-induced active sites, thereby suppressing structural degradation during prolonged electrochemical operation.

2.3. Test for Performance of Assembled ZABs

To evaluate the feasibility of CNP in practical energy storage devices, a liquid ZAB was constructed, adopting CNP as the air cathode, polished zinc foil as the anode, and an alkaline electrolyte composed of 6.0 M KOH mixed with 0.2 M $Zn(OAc)_2$ (Figure 5a). In addition, a Pt/C-based ZAB was constructed as a benchmark for comparison. As illustrated in Figure 5b, the CNP-based ZAB exhibits a superior open-circuit voltage (OCV) of 1.52 V, lightly higher than that of the Pt/C device (1.48 V), indicating favorable thermodynamic and interfacial characteristics. Notably, the assembled battery successfully powers an LED array (inset of Figure 5b), demonstrating its practical applicability. The discharge polarization and power density curves (Figure 5c) reveal that the

https://doi.org/10.1021/acsanm.6c02496
ACS Appl. Nano Mater. XXXX, XXX, XXX−XXX

CNP-based ZAB achieves a remarkable peak power density of 202.2 mW cm^{-2}, substantially exceeding that of Pt/C-based counterpart (130.3 mW cm^{-2}). Furthermore, a stable discharge plateau is maintained over a broad current density range (2−20 mA cm^{-2}). Notably, the discharge potential exhibits complete recovery upon returning to the initial current density of 2 mA cm^{-2} (Figure 5d), demonstrating excellent rate capability and electrochemical reversibility. At a current density of 5 mA cm^{-2}, the CNP-based ZAB delivers a high specific capacity of 768.8 mA h g_{Zn}^{-1}, outperforming the Pt/C-based ZAB (698.9 mA h g_{Zn}^{-1}) (Figure 5e). Importantly, a comparative analysis (Figure 5f and Table S4) further confirms that the CNP-based device ranks among the best-performing metal-free ORR catalysts reported to date, with both power density and capacity.

Given the relatively limited oxygen evolution reaction (OER) activity of CNP (594 mV @ 20 mA cm^{-2}, Figure S16), RuO_2 was introduced as an OER catalyst to construct a rechargeable ZAB, following the widely adopted strategy of combining ORR and OER catalysts for bifunctional performance.[60] The CNP+RuO_2-based battery retained excellent cycling durability, maintaining continuous operation exceeding 206 h. In contrast, the Pt/C+RuO_2-based ZAB underwent rapid degradation after approximately 120 h (Figure 5g), attesting to the remarkable architectural resilience and enduring electrochemical durability of the CNP catalyst under prolonged cycling conditions. To further evaluate flexibility and applicability in wearable electronics, a solid-state flexible ZAB was fabricated through a layered configuration, using a PVA hydrogel electrolyte saturated with KOH and $Zn(OAc)_2$, with catalyst-coated carbon cloth as the cathode, zinc foil as the anode, and nickel foam as the current collector (Figure 5h). The CNP-based flexible ZAB exhibits an OCV of 1.35 V, comparable to that of the Pt/C-based device (1.36 V) (Figure 5i). Notably, the discharge polarization curve (Figure 5j) demonstrates that the CNP-based device delivers a peak power density of 67.5 mW cm^{-2}, significantly higher than that of the Pt/C benchmark (49.6 mW cm^{-2}). Additionally, the CNP-based flexible ZAB maintains a stable output voltage at bending angles of 0°, 30°, 60°, and 90° (Figure 5k), demonstrating excellent mechanical durability and structural integrity. Collectively, the superior OCV, high power density, enhanced specific capacity, outstanding cycling durability, and mechanical flexibility validate the effectiveness of N/P codoped CNP as a high-performance metal-free air cathode for both liquid and flexible ZABs.

3. CONCLUSIONS

In this work, a nanowrinkled N/P codoped carbon-sphere electrocatalyst was successfully prepared, synergistically integrating defect engineering, hierarchical mesoporosity, and enhanced electronic modulation within a robust carbon framework. The optimized structure yields a half-wave potential of 0.85 V and a low Tafel slope of 80 mV dec^{-1}, with a kinetic current density of 13.1 mA cm^{-2} at 0.8 V and a dominant four-electron ORR pathway. The impressive catalytic behavior can be credited to the N/P codoped mesoporous architecture, which not only provides plentiful active sites and accelerates electron/mass transport but also facilitates electrolyte permeation, thereby enhancing the overall ORR process. XPS further reveals that N−P codoping significantly increases the relative content of pyridinic/pyrrolic nitrogen in CNP, fine-tuning the O_2 adsorption/desorption behavior and thus enhancing the intrinsic catalytic activity. In practical devices, the CNP-based liquid ZAB achieves a peak power density of 202.2 mW cm^{-2} and a specific capacity of 768.8 mA h g_{Zn}^{-1}, surpassing Pt/C benchmarks. The rechargeable configuration demonstrates stable cycling for over 206 h, while the flexible ZAB delivers 67.5 mW cm^{-2} and maintains stable output under mechanical deformation. This work provides novel insights into the design of synergistic N/P electronic modulation and nanoarchitectural engineering in advancing durable, high-power, metal-free cathodes for next-generation ZABs.

■ ASSOCIATED CONTENT

Supporting Information

The Supporting Information is available free of charge at https://pubs.acs.org/doi/10.1021/acsanm.6c02496.

Detailed synthesis procedures; XRD patterns; Raman spectra; N_2 adsorption−desorption isotherm; electrochemical measurements including CV, LSV, Tafel slopes, ECSA, EIS, and stability tests (PDF)

■ AUTHOR INFORMATION

Corresponding Authors

Tayirjan Taylor Isimjan − *Saudi Arabia Basic Industries Corporation (SABIC) at King Abdullah University of Science and Technology (KAUST), Thuwal 23955-6900, Saudi Arabia*; Email: isimjant@sabic.com

Lixia Wang − *Shenzhen Key Laboratory of Micro/nano-Porous Functional Materials (SKLPM) and Department of Chemistry, Southern University of Science and Technology, Shenzhen 518055, China*; Email: wanglx6@sustech.edu.cn

Xiulin Yang − *Guangxi Key Laboratory of Low Carbon Energy Materials, School of Chemistry and Pharmaceutical Sciences, Guangxi Normal University, Guilin 541004, China*; orcid.org/0000-0003-2642-4963; Email: xlyang@gxnu.edu.cn

Authors

Jiasui Huang − *Guangxi Key Laboratory of Low Carbon Energy Materials, School of Chemistry and Pharmaceutical Sciences, Guangxi Normal University, Guilin 541004, China*

Bowen Yao − *Guangxi Key Laboratory of Low Carbon Energy Materials, School of Chemistry and Pharmaceutical Sciences, Guangxi Normal University, Guilin 541004, China*

Zhiyang Huang − *Guangxi Key Laboratory of Low Carbon Energy Materials, School of Chemistry and Pharmaceutical Sciences, Guangxi Normal University, Guilin 541004, China*

Complete contact information is available at: https://pubs.acs.org/10.1021/acsanm.6c02496

Author Contributions

J.H.: Investigation, Conceptualization, Writing—original draft. B.Y.: Data curation. Z.H.: Methodology. T.T.I.: Writing—review and editing. L.W.: Supervision, Writing—review and editing. X.Y.: Supervision, Writing—review and editing.

Notes

The authors declare no competing financial interest.

https://doi.org/10.1021/acsanm.6c02496
ACS Appl. Nano Mater. XXXX, XXX, XXX−XXX

■ ACKNOWLEDGMENTS

This work was financially supported by the Guangxi Science and Technology Projects (GUIKE LT2600640010), the Natural Science Foundation of Guangxi Province (2026GXNSFBA00640178), and the National Natural Science Foundation of China (52363028; W2621022; 21965005).

■ REFERENCES

(1) Xie, Y.; Feng, Y.; Zhu, S.; Yu, Y.; Bao, H.; Liu, Q.; Luo, F.; Yang, Z. Modulation in Spin State of Co_3O_4 Decorated Fe Single Atom Enables a Superior Rechargeable Zinc-Air Battery Performance. *Adv. Mater.* **2025**, *37* (5), No. e2414801.

(2) He, B.; Zhang, Q.; Pan, Z.; Li, L.; Li, C.; Ling, Y.; Wang, Z.; Chen, M.; Wang, Z.; Yao, Y.; Li, Q.; Sun, L.; Wang, J.; Wei, L. Freestanding Metal-Organic Frameworks and Their Derivatives: An Emerging Platform for Electrochemical Energy Storage and Conversion. *Chem. Rev.* **2022**, *122* (11), 10087−10125.

(3) Wang, J.; Hu, S. Delocalized electron engineering in metal-air batteries: formation mechanisms, regulation strategies, and applications. *Coord. Chem. Rev.* **2026**, *548*, 217214.

(4) Liu, Q.; Chen, J.; Cao, L.; Wang, Y.; Qi, Y.; Wei, Y.; Ma, Q.; Huang, J.; Fan, X.; Feng, Y. Electronic Communication Between Single Atomic Nickel and Iron-Nitrogen Species Promote the Bifunctional Oxygen Evolution and Reduction for Efficient Rechargeable Zinc-Air Battery. *Adv. Funct. Mater.* **2025**, *35* (25), No. e2424597.

(5) Wu, S.; Liu, X.; Mao, H.; Zhu, J.; Zhou, G.; Chi, J.; Wu, Z.; Wang, L. Unraveling the Tandem Effect of Nitrogen Configuration Promoting Oxygen Reduction Reaction in Alkaline Seawater. *Adv. Energy Mater.* **2024**, *14* (24), No. e2400183.

(6) Yang, L.; Zhu, Y.; Yao, X.; Du, C.; Han, Z.; Tian, J.; Liu, X.; Ma, X.; Cao, C. Surface-optimized carbon nanocages with tailorable atomic Fe-N_4 sites to boost oxygen reduction in long stable zinc-air battery. *Energy Storage Mater.* **2023**, *63*, 102972.

(7) Zhou, Y.; Lu, R.; Tao, X.; Qiu, Z.; Chen, G.; Yang, J.; Zhao, Y.; Feng, X.; Müllen, K. Boosting Oxygen Electrocatalytic Activity of Fe-N-C Catalysts by Phosphorus Incorporation. *J. Am. Chem. Soc.* **2023**, *145* (6), 3647−3655.

(8) Lyu, C.; Yang, J.; Guo, H.; Cheng, J.; Geng, D.; Liu, Y. Co-based bifunctional OER/ORR electrocatalysts: From nanostructure engineering to catalytic mechanism innovation for cutting-edge research in empowering energy conversion systems. *Coord. Chem. Rev.* **2026**, *551*, 217393.

(9) Yu, Q.; Liu, X.; Liu, G.; Wang, X.; Li, Z.; Li, B.; Wu, Z.; Wang, L. Constructing Three-Phase Heterojunction with 1D/3D Hierarchical Structure as Efficient Trifunctional Electrocatalyst in Alkaline Seawater. *Adv. Funct. Mater.* **2022**, *32* (46), No. e2205767.

(10) Yang, J.; Wang, Y.; Zhao, X.; Kang, J.; Zhou, X.; Ma, L.; Yang, Y.; Jiang, R. Atomically Dispersed Fe-N_4 Bridged with MoO_x Clusters as a Bifunctional Electrocatalyst for Rechargeable Zn-Air Battery. *Adv. Funct. Mater.* **2025**, *35* (9), No. e2416215.

(11) Ku, Y.-P.; Ehelebe, K.; Hutzler, A.; Bierling, M.; Böhm, T.; Zitolo, A.; Vorokhta, M.; Bibent, N.; Speck, F. D.; Seeberger, D.; Khalakhan, I.; Mayrhofer, K. J. J.; Thiele, S.; Jaouen, F.; Cherevko, S. Oxygen Reduction Reaction in Alkaline Media Causes Iron Leaching from Fe-N-C Electrocatalysts. *J. Am. Chem. Soc.* **2022**, *144* (22), 9753−9763.

(12) Zhang, L.; Dong, Y.; Li, L.; Shi, Y.; Zhang, Y.; Wei, L.; Dong, C.-L.; Lin, Z.; Su, J. Concurrently Boosting Activity and Stability of Oxygen Reduction Reaction Catalysts via Judiciously Crafting Fe−Mn Dual Atoms for Fuel Cells. *Nano Micro Lett.* **2025**, *17* (1), 88.

(13) Pedersen, A.; Kumar, K.; Ku, Y.-P.; Martin, V.; Dubau, L.; Santos, K. T.; Barrio, J.; Saveleva, V. A.; Glatzel, P.; Paidi, V. K.; Li, X.; Hutzler, A.; Titirici, M.-M.; Bonnefont, A.; Cherevko, S.; Stephens, I. E. L.; Maillard, F. Operando Fe dissolution in Fe-N-C electrocatalysts during acidic oxygen reduction: impact of local pH change. *Energy Environ. Sci.* **2024**, *17* (17), 6323−6337.

(14) Zhao, Y.; Huang, M.; Kang, Y.; Fang, Y.; Zhao, T.; Wang, H.; Ou, J.; Liu, J.; Zhong, M.; Wang, T.; Sun, X.; Zhao, C.; Wang, D. Ligand effects enhancing low-temperature oxygen reduction kinetics in neutral conditions. *Energy Environ. Sci.* **2025**, *18* (11), 5298−5308.

(15) Wang, X.; Yu, M.; Feng, X. Electronic structure regulation of noble metal-free materials toward alkaline oxygen electrocatalysis. *eScience* **2023**, *3* (4), 100141.

(16) Guo, W.; Wan, Y.; Xiao, Z.; Zhang, M.; Lin, Y. Beyond the N-doping controversy: Molecularly deciphering the active origins in metal-free carbon for electrocatalytic oxygen reduction reaction. *J. Energy Chem.* **2025**, *111*, 420−429.

(17) Zhang, Z.; Zhang, F.; Song, Z.; Zhang, L. Oxygen Reduction Reaction on Pyridinic Nitrogen-Functionalized Carbon: Active Site Quantification and Effects of Lewis Basicity. *ACS Catal.* **2025**, *15* (1), 296−309.

(18) Pakrieva, E.; Hernandez-Ferrer, J.; Martinez, G.; Balas, F.; García-Bordeje, E.; Anson-Casaos, A.; Simonelli, L.; Bartolome, F.; Benito, A. M.; Maser, W. K.; Hueso, J. L.; Santamaria, J. 3-component (N, Fe, Co). atomically dispersed ORR catalysts prepared by laser-driven decomposition of organic precursors. *Chem. Eng. J.* **2025**, *526*, 171198.

(19) Feng, X.; Bai, Y.; Liu, M.; Li, Y.; Yang, H.; Wang, X.; Wu, C. Untangling the respective effects of heteroatom-doped carbon materials in batteries, supercapacitors and the ORR to design high performance materials. *Energy Environ. Sci.* **2021**, *14* (4), 2036−2089.

(20) Wei, P.; Li, X.; He, Z.; Sun, X.; Liang, Q.; Wang, Z.; Fang, C.; Li, Q.; Yang, H.; Han, J.; Huang, Y. P. N. B co-doped carbon nanotubes as efficient metal-free electrocatalysts for ORR and Zn-air batteries. *Chem. Eng. J.* **2021**, *422*, 130134.

(21) Guo, K.; He, Z.; Lu, S.; Zhang, P.; Li, N.; Bao, L.; Yu, Z.; Song, L.; Lu, X. A Fullerene Seeded Strategy for Facile Construction of Nitrogen-Doped Carbon Nano-Onions as Robust Electrocatalysts. *Adv. Funct. Mater.* **2023**, *33* (29), No. e2302100.

(22) Xia, H.; Sun, M.; Yang, D.; Pang, R.; Zeng, Q.; Huang, L.; Huang, B.; Li, J.; Wang, E. Phosphorus/Sulfur-Modulated p-Band Center of Pentagonal Carbon for Efficient Oxygen Reduction Reaction. *J. Am. Chem. Soc.* **2025**, *147* (45), 41472−41480.

(23) Ao, K.; Yue, X.; Zhang, X.; Zhao, H.; Liu, J.; Shi, J.; Daoud, W. A.; Li, H. N-P covalent bond regulation of mesoporous carbon-based catalyst for lowered oxygen reduction overpotential and enhanced zinc-air battery performance. *J. Colloid Interface Sci.* **2024**, *672*, 107−116.

(24) Gao, J.; Wang, G.; Wang, W.; Yu, L.; Peng, B.; El-Harairy, A.; Li, J.; Zhang, G. Engineering electronic transfer dynamics and ion adsorption capability in dual-doped carbon for high-energy potassium ion hybrid capacitors. *ACS Nano* **2022**, *16* (4), 6255−6265.

(25) Li, Z.; Ji, S.; Liu, H.; Xu, C.; Guo, C.; Lu, X.; Sun, H.; Dou, S.; Xin, S.; Horton, J. H.; et al. Constructing Asymmetrical Coordination Microenvironment with Phosphorus-Incorporated Nitrogen-Doped Carbon to Boost Bifunctional Oxygen Electrocatalytic Activity. *Adv. Funct. Mater.* **2024**, *34* (18), No. e2314444.

(26) Yu, X.; Kim, H. J.; Hong, J.-Y.; Jung, Y. M.; Kwon, K. D.; Kong, J.; Park, H. S. Elucidating surface redox charge storage of phosphorus-incorporated graphenes with hierarchical architectures. *Nano Energy* **2015**, *15*, 576−586.

(27) Hu, H.; Xu, Z.; Zhang, Z.; Yan, X.; Zhu, Y.; Attfield, J. P.; Yang, M. Electrocatalytic Oxygen Reduction Using Metastable Zirconium Suboxide. *Angew. Chem., Int. Ed.* **2024**, *63* (30), No. e202404374.

(28) Cui, B.; Zhu, Y.; Fang, X.; Du, R.; Bai, J.; Li, M.; Xiang, W.; Xie, W.; Liu, Y.; Zhang, J.; Shi, R.; Wang, J.; Yang, J. Dual-phase Co/CoFe nanoparticles anchored on N, F co-doped hollow carbon microcapsules as efficient bifunctional catalysts for aqueous/quasi-solid-state Zn-air batteries. *Chem. Eng. J.* **2026**, *534*, 175339.

(29) Shao, Y.; Yang, Q.; Zhang, Y.; Jiang, N.; Hao, Y.; Qu, K.; Du, Y.; Qi, J.; Li, Y.; Tang, Y.; Lu, X.; Zhang, L.; Qiu, J. A Universal Method for Regulating Carbon Microcrystalline Structure for High-Capacity Sodium Storage: Binding Energy As Descriptor. *ACS Nano* **2023**, *17* (23), 24012−24021.

https://doi.org/10.1021/acsanm.6c02496
ACS Appl. Nano Mater. XXXX, XXX, XXX−XXX

(30) Gong, T.; Qi, R.; Liu, X.; Li, H.; Zhang, Y. N. N, F-Codoped Microporous Carbon Nanofibers as Efficient Metal-Free Electrocatalysts for ORR. *Nano Micro Lett.* **2019**, *11* (1), 9.
(31) Shu, X.; Wang, Y.; Ma, K.; Yang, C.; Chen, X.; He, B.; Ma, J.; Zhang, J. Synergistic Phosphorus Modification of Iron-Nitrogen-Carbon Electrocatalysts for Durable Rechargeable Zinc-air Batteries. *CCS Chem.* **2026**, *8* (3), 1568−1579.
(32) Liu, Z.-W.; Peng, F.; Wang, H.-J.; Yu, H.; Zheng, W.-X.; Yang, J. Phosphorus-doped graphite layers with high electrocatalytic activity for the O_2 reduction in an alkaline medium. *Angew. Chem., Int. Ed.* **2011**, *50* (14), 3257−3261.
(33) Luo, T.; Jia, F.; Liang, J.; Yu, Z.; Wang, P.; Chen, H.; Zhu, P.; Long, Z.; Zhao, X.; Liu, S. Multiscale engineering of N-CoP@NC/3D-NC bifunctional electrocatalyst: Synergistic interface and doping design for high-performance zinc-air batteries. *Small* **2026**, *22* (11), No. e13939.
(34) Lei, W.; Deng, Y.-P.; Li, G.; Cano, Z. P.; Wang, X.; Luo, D.; Liu, Y.; Wang, D.; Chen, Z. Two-Dimensional Phosphorus-Doped Carbon Nanosheets with Tunable Porosity for Oxygen Reactions in Zinc-air Batteries. *ACS Catal.* **2018**, *8* (3), 2464−2472.
(35) Sheng, Z.-H.; Shao, L.; Chen, J.-J.; Bao, W.-J.; Wang, F.-B.; Xia, X.-H. Catalyst-free synthesis of nitrogen-doped graphene via thermal annealing graphite oxide with melamine and its excellent electrocatalysis. *ACS Nano* **2011**, *5* (6), 4350−4358.
(36) Zhao, Q.; Tan, X.; Liu, T.; Hou, S.; Ni, W.; Huang, H.; Zhang, J.; Yang, Z.; Li, D.; Hu, H.; Wu, M. E. A. N. P and S active sites on hierarchical porous carbon nanoshells for superior oxygen reduction reaction and rechargeable Zn-air batteries. *J. Colloid Interface Sci.* **2023**, *633*, 1022−1032.
(37) Su, J.; Wan, Y.; Feng, L.; Huang, D.; Chu, H. K.; Zhang, X.; Geng, X.; Wang, Y.; Zhong, R.; Zou, R. "One-stone, Two-birds": Zinc-rich metal-organic frameworks as precursors for high-entropy Zn-air battery electrocatalysts with hierarchical pore structures. *Angew. Chem., Int. Ed.* **2025**, *64* (1), No. e202413826.
(38) Rana, D. S.; Sharma, R.; Awasthi, A.; Singh, D.; Sharma, A. Biomass-derived phosphorus-doped nanocarbon: A metal-free electrode for high-performance supercapacitors. *J. Energy Storage* **2025**, *131*, 117586.
(39) An, L.; Zhu, J.; Yang, J.; Wang, D. Tailoring the d-band center of iridium-doped cobalt selenide for dual-boosted hydrogen and oxygen evolution reactions. *Nano Mater. Sci.* **2026**, *8* (3), 703−709.
(40) Long, Y.; Ye, F.; Shi, L.; Lin, X.; Paul, R.; Liu, D.; Hu, C. N. and S tri-doped holey carbon as an efficient electrocatalyst for oxygen reduction in whole pH range for fuel cell and zinc-air batteries. *Carbon* **2021**, *179*, 365−376.
(41) Yang, Y.; Shi, L.; Liang, Q.; Liu, Y.; Dong, J.; Isimjan, T. T.; Wang, B.; Yang, X. Uleashing efficient and CO-resilient alkaline hydrogen oxidation of Pd_3P through phosphorus vacancy defect engineering. *Chin. J. Catal.* **2024**, *56*, 176−187.
(42) Gao, L.; Ying, D.; Shen, T.; Zheng, Y.; Cai, J.; Wang, D.; Zhang, L. Two-Dimensional Wrinkled N-Rich Carbon Nanosheets Fabricated from Chitin via Fast Pyrolysis as Optimized Electrocatalyst. *ACS Sustainable Chem. Eng.* **2020**, *8* (29), 10881−10891.
(43) Wu, Y.; Zhang, Y.; Lan, L.; Hu, T.; Tang, S.; Lützenkirchen-Hecht, D.; Yuan, K.; Chen, Y. Engineering Proton-Coupled Electron Transfer to Break Activity-Stability Trade-Off of Oxygen Electroreduction Catalysts for Temperature-Adaptive Zn−Air Battery. *Angew. Chem., Int. Ed.* **2025**, *64* (22), No. e202502019.
(44) Jiang, Z.-J.; Jiang, Z. Fabrication of Nitrogen-Doped Holey Graphene Hollow Microspheres and Their Use as an Active Electrode Material for Lithium Ion Batteries. *ACS Appl. Mater. Interfaces* **2014**, *6* (21), 19082−19091.
(45) Hong, C.; Zhang, Y.; Huang, S.; Sha, L.; Xu, M.; Ma, Y.; Li, Y.; Han, X. Synergistic pyridinic-N/pyrrolic-N coordination tailors cobalt electronic states for high-efficiency oxygen reduction in Zn-air batteries. *J. Mater. Chem. A* **2025**, *13* (37), 31720−31726.
(46) Kim, K.; Kim, G.; Jeong, T.; Lee, W.; Yang, Y.; Kim, B.-H.; Kim, B.; Lee, B.; Kang, J.; Kim, M. Activating the Mn Single Atomic Center for an Efficient Actual Active Site of the Oxygen Reduction Reaction by Spin-State Regulation. *J. Am. Chem. Soc.* **2024**, *146* (49), 34033−34042.
(47) Zeng, Y.; Wang, X.; Qi, W.; Liu, C.; Lu, L.; Xiao, M.; Li, K.; Xiao, F.; Shao, M.; Xing, W.; et al. Aligned d-orbital energy level of dual-atom sites catalysts for oxygen reduction reaction in anion exchange membrane fuel cells. *Nat. Commun.* **2025**, *16* (1), 8111.
(48) Poon, K. C.; Wan, W. Y.; Su, H.; Sato, H. One-Minute Synthesis via Electroless Reduction of Amorphous Phosphorus-Doped Graphene for Oxygen Reduction Reaction. *ACS Appl. Energy Mater.* **2021**, *4* (6), 5388−5391.
(49) Wu, Z.; Gao, Y.; Wang, Z.; Xiao, W.; Wang, X.; Li, B.; Li, Z.; Liu, X.; Ma, T.; Wang, L. Surface-enriched ultrafine Pt nanoparticles coupled with defective CoP as efficient trifunctional electrocatalyst for overall water splitting and flexible Zn-air battery. *Chin. J. Catal.* **2023**, *46*, 36−47.
(50) Zhao, Y.-X.; Wen, J.-H.; Li, P.; Zhang, P.-F.; Wang, S.-N.; Li, D.-C.; Dou, J.-M.; Li, Y.-W.; Ma, H.-Y.; Xu, L. A "Pre-Division Metal Clusters" Strategy to Mediate Efficient Dual-Active Sites ORR Catalyst for Ultralong Rechargeable Zn-Air Battery. *Angew. Chem., Int. Ed.* **2023**, *62* (11), No. e202216950.
(51) Chen, J.; Shi, X.; Feng, S.; Li, J.; Gao, X.; Wu, X.; Li, K.; Qi, A.; You, C.; Tian, X. Design of highly active and durable oxygen evolution catalyst with intrinsic chlorine inhibition property for seawater electrolysis. *Nano Mater. Sci.* **2024**, *6* (4), 413−418.
(52) Liu, M.; Liang, B.; Liang, Y.; Peng, Y.; Lin, Y.; Wang, Z.; Wang, Y.; Tan, Z.; Yang, Y.; Xi, H.; Li, J.; Duan, C. Two-dimensional CoS/Co-MOF Composite Electrocatalyst for Efficient Oxygen Evolution Reaction. *ECS* **2025**, *1* (3), 9600052.
(53) Xiang, Y.; Wen, J.-H.; Zhao, Y.-X.; Li, P.; Li, M.-Q.; Ren, Y.-T.; Wang, S.-N.; Dou, J.-M.; Li, Y.-W.; Ma, H.-Y.; et al. A "Dual Spatial Confinement" Route to Tailor Efficient Dual-Active Sites ORR Catalyst for Rechargeable Zn-Air Batteries. *Small* **2025**, *21* (32), No. e2504022.
(54) Liu, B.; Pan, W.; Huang, Z.; Zhao, Y.; Luo, Z.; Isimjan, T. T.; Wang, B.; Yang, X. Unlocking 5300-h ultrastable metal-free ORR catalysts for Zn-air batteries via F−N co-doped tailored carbon pore architectures and synergistic adsorption modulation. *Chin. J. Catal.* **2025**, *79*, 100−111.
(55) Liu, F.; Zhang, S.; Ma, S.; Cao, Z.; Li, Y.; Ma, Y.; Xu, X.; Zhang, J.; Xue, Y.; Tang, C. Enhanced oxygen reduction reaction performance in boron carbon nitride through P doping for zinc-air batteries. *Appl. Surf. Sci.* **2025**, *710*, 163913.
(56) Guo, Z.; Yang, S.; Liu, M.; Xu, Q.; Zeng, G. Construction of imide-linked covalent organic frameworks with palladium nanoparticles for oxygen reduction reaction. *EcoEnergy* **2024**, *2* (1), 192−201.
(57) Ud Din, M. A.; Idrees, M.; Jamil, S.; Irfan, S.; Nazir, G.; Mudassir, M. A.; Saleem, M. S.; Batool, S.; Cheng, N.; Saidur, R. Advances and challenges of methanol-tolerant oxygen reduction reaction electrocatalysts for the direct methanol fuel cell. *J. Energy Chem.* **2023**, *77*, 499−513.
(58) Li, P.; Wen, J.; Xiang, Y.; Li, M.; Zhao, Y.; Wang, S.; Dou, J.; Li, Y.; Ma, H.; Xu, L. Hierarchical mesoporous N-doped carbon as an efficient ORR/OER bifunctional electrocatalyst for rechargeable zinc−air battery. *Inorg. Chem. Front.* **2024**, *11* (16), 5345−5358.
(59) Ren, Y.-T.; Yuan, Y.-Y.; Xiang, Y.; Zhao, H.; Hao, H.-G.; Ma, H.-Y.; Wang, S.-N.; Li, Y.-W. Coupling of metallic Co with atomic Co−N−C as efficient bifunctional oxygen electrocatalyst for rechargeable zinc-air battery. *J. Alloys Compd.* **2025**, *1044*, 184447.
(60) Li, Y.-W.; Zhang, W.-J.; Li, J.; Ma, H.-Y.; Du, H.-M.; Li, D.-C.; Wang, S.-N.; Zhao, J.-S.; Dou, J.-M.; Xu, L. Fe-MOF-Derived Efficient ORR/OER Bifunctional Electrocatalyst for Rechargeable Zinc−Air Batteries. *ACS Appl. Mater. Interfaces* **2020**, *12* (40), 44710−44719.

https://doi.org/10.1021/acsanm.6c02496
ACS Appl. Nano Mater. XXXX, XXX, XXX−XXX